# Cyanometallic frameworks derived hierarchical porous Fe$_2$O$_3$/NiO microflowers with excellent lithium-storage property

Yingying Chen [a, b], Rong Cai [b], Yang Yang [b], Chun Liu [b], Aihua Yuan [b], Hongxun Yang [b], Xiaoping Shen [a, *]

[a] School of Chemistry & Chemical Engineering, School of Material Science & Engineering, Jiangsu University, Zhenjiang 212013, PR China
[b] School of Environmental & Chemical Engineering, Jiangsu University of Science and Technology, Zhenjiang 212003, PR China

ABSTRACT

Hierarchical porous microflowers composed of porous Fe$_2$O$_3$/NiO nanoplates were synthesized via a facile cyanometallic framework-templated strategy. The synthesized Fe$_2$O$_3$/NiO microflowers were characterized by X-ray powder diffraction, scanning electron microscopy, transmission electron microscopy and Brunauer Emmet Teller adsorption-desorption analysis. As anode materials for lithium ion batteries, the Fe$_2$O$_3$/NiO microflowers exhibit excellent electrochemical performance in terms of great lithium storage capacity (1652.6 mAh g$^{-1}$ at 100 mA g$^{-1}$) and good cycling stability (1210.4 mAh g$^{-1}$ capacity retention at 50th cycle). This result can be attributed to the hierarchical porous structure of the Fe$_2$O$_3$/NiO microflowers, which could increase active sites for lithium ions storage, accommodate the volume expansion/contraction during charge-discharge cycles, and the synergistic effect between Fe$_2$O$_3$ and NiO.

© 2016 Elsevier B.V. All rights reserved.

## 1. Introduction

Lithium ion batteries (LIBs), as a type of high efficient green energy storage system, have been widely applied to portable electronic devices, stationary energy storage systems as well as rapidly developing electric vehicles [1—4]. However, the current commercial LIBs with graphite as anode with a theoretical capacity of 372 mAh g$^{-1}$ cannot meet requirement for more demanding applications due to the limitations in energy capacity and reliable operation. In recent years, transition metal oxides such as SnO$_2$ [5,6], Fe$_2$O$_3$ [7—11], NiO [12—14], Mn$_3$O$_4$ [15], and Co$_3$O$_4$ [16—20] have been extensively studied as LIBs anode materials because of their higher specific capacity and volumetric energy density. Especially, the theoretical capacities of Fe$_2$O$_3$ and NiO are as high as 1007 and 718 mAh g$^{-1}$, respectively, which are approximately 2—3 times higher than that of conventional graphite anode. However, almost all transitional metal oxides including iron oxide and nickel oxide often show low initial coulombic efficiency, poor cycling stability and rate performance due to their large volume expansion/contraction during the lithium insertion and extraction process.

One promising solution is to construct porous and/or hierarchical nanostructures to improve electrochemical performance of electrode and maintain structural integrity. For instance, Zhang et al. synthesized mesoporous Fe$_2$O$_3$ nanoparticles with an excellent cycling performance (1009 mA h g$^{-1}$ at 230 cycles at a current density of 100 mA g$^{-1}$) [21]. Wang et al. reported that the porous NiO microtubes as LIBs anode material exhibited excellent performance with 640 mA h g$^{-1}$ after 200 cycles at 1 A g$^{-1}$ [22]. Lou et al. synthesized Fe$_2$O$_3$ microboxes with hierarchically structured shells by annealing PB microcubes in air, delivering high reversible capacity of 945 mA h g$^{-1}$ at a current density of 200 mA g$^{-1}$ after 30 cycles [23]. In addition, composite nanomaterials that integrate two different metal oxides have also been demonstrated to deliver unique lithium storage performance compared to their individual counterparts. By combining specific properties of different components, electrochemical performance can be greatly improved in such composite electrodes [24—28]. For example, multilayer CuO@NiO hollow microsphere delivered a larger-than-theoretical reversible capacity of 1061 mAh g$^{-1}$ after 200 cycles at 100 mA g$^{-1}$, which is very outstanding among various NiO or CuO electrode structures [29]. The porous nanocubes of SnO$_2$-Fe$_2$O$_3$ mixed oxides also exhibited high lithium storage capacity (1020.2 mA h g$^{-1}$ at 200 mA g$^{-1}$) and excellent cycling performance [30]. Therefore, development of hierarchical porous architectures

integrated different metal oxide components is a promising approach to advanced oxide anodes with enhanced lithium-storage performance.

Until now, many strategies have been developed to prepare porous and/or hierarchical nanostructured metal oxides. Among them, template method, primarily by thermal decomposition of corresponding precursors such as hydroxides, carbonates, metal organic frameworks, etc. has been demonstrated to be a highly effective approach to porous and/or hierarchical oxide nanostructure with well-defined morphology and high uniformity [31—33]. Especially, cyanometallic frameworks (CMFs) such as Prussian blue (PB) and Prussian blue analogues (PBA) have been demonstrated to be a new class of template/precursors for porous/hierarchical metal oxide syntheses because of their special thermal properties, unique reactivity and highly tailor ability [34,35]. With proper CMFs precursors, bi- or even multi-component mixed metal oxides with porous/hierarchical nanostructures can be easily obtained, which provides a unique chance to develop a new family of highly tailored oxide functional materials [36,37].

Herein, we present a facile approach for the synthesis of hierarchical porous $Fe_2O_3/NiO$ nanocomposites by using CMFs precursor of $Fe(H_2O)_2[Ni(CN)_4]$. The well-defined flower-like $Fe_2O_3/NiO$ architectures, which are constructed by porous nanoplates with highly uniform composition, are obtained by simply annealing the precursor. The electrochemical characteristics of the as-prepared $Fe_2O_3/NiO$ composites are investigated as LIBs anode materials, and exhibit remarkably improved reversible capacity and cycling stability.

## 2. Experimental

### 2.1. Materials

All the chemical reagents used in our research were of analytical grade and used without further purification. Deionized water was used throughout the experiments.

### 2.2. Synthesis of flower-like $Fe(H_2O)_2[Ni(CN)_4]$ precursor

In a typical synthesis, 1 mmol of $K_2[Ni(CN)_4]$ was dissolved in 40 mL of aqueous solution of polyethylene glycol (PEG) (0.06 g) with stirring, and then 40 mL of aqueous solution of $FeSO_4$ (1 mmol) was added in. The resulting mixture was ultrasonically treated for 1 h at room temperature, and a pale yellow suspension was formed. The pale yellow precipitate was isolated by centrifugation, washed several times with deionized water, and dried at 65 °C overnight.

### 2.3. Synthesis of hierarchical porous $Fe_2O_3/NiO$ microflowers

The flower-like $Fe_2O_3/NiO$ composites with porous structure were obtained by annealing the flower-like precursor of $Fe(H_2O)_2[Ni(CN)_4]$ at 650 °C for 1 h in air with a heating rate of 1 °C $min^{-1}$.

### 2.4. Materials characterizations

The phase structures of the as-synthesized samples were characterized by XRD (Rigaku D/MAX RINT-2000, Cu Kα radiation). The morphology and composition were examined by scanning electron microscopy (SEM, JSM-840A and JSM-6700 F) equipped with an energy dispersive spectrometry (EDS). The microstructures of the samples were investigated by transmission electron microscopy (TEM, JEM-2100). The specific surface area and pore size distribution were measured by Micromeritics ASAP2020 using $N_2$

adsorption-desorption isotherms. Thermogravimetric (TG) analysis was performed using a Perkin-Elmer Diamond TG/DTA instrument in air at a heating rate of 10 °C $min^{-1}$.

### 2.5. Electrochemical measurements

Electrochemical measurement was carried out using CR2032-type coin cells with ENTEK ET20-26 membrane as separator and lithium-foil as counter electrode. The cell assembly was carried out in an Ar-filled glovebox with moisture and oxygen concentrations below 1 ppm. The working electrode was prepared by mixing the synthesized active materials, acetylene black, and polyvinylidene fluoride (PVDF) in a mass ratio of 80:10:10 with N-methyl pyrrolidinone (NMP) as a solvent. After stirred for 24 h, the mixture was then painted on a copper foil, and dried at 120 °C under vacuum for 12 h. The electrolyte was 1 M $LiPF_6$ in the mixture of ethylene carbonate (EC) and dimethyl carbonate (DMC) (1:1 in volume ratio), plus 2 wt% vinylene carbonate (VC). The total mass of the active electrode material is about 1.2—1.5 mg and the electrode surface area is 1.54 $cm^2$ (Φ 14 mm). The cells were tested on a LAND battery test system (Wuhan Kingnuo Electronics Co., Ltd., China) within the voltage range of 0.01—3.0 V vs. $Li^+/Li$. Cyclic voltammetry (CV) measurements were performed on the $Fe_2O_3$ microflower working electrode using an electrochemical workstation (Autolab 302 N) between 3.0 and 0.01 vs ($Li/Li^+$)/V at a sweep rate of 0.2 mV $s^{-1}$. Electrochemical impedance spectroscopy (EIS) tests were also measured on an electrochemical workstation (Autolab 302 N) operating in the frequency range of 0.1 Hz—$10^6$ Hz with ac amplitude of 10 mV.

## 3. Results and discussion

### 3.1. Characterizations of hierarchical porous $Fe_2O_3/NiO$ microflowers

The hierarchical porous microflowers of $Fe_2O_3/NiO$ can be achieved via a facile ultrasonic method followed by a calcination treatment. The morphology and size of the precursor were characterized by SEM. As seen from Fig. 1a, the precursor shows a flower-like hierarchical architecture with a diameter of ca. 5 μm. The magnified view in Fig. 1b revealed that the flowers were assembled by many densely packed nanoplates with ca. 100 nm thickness, and these nanoplates grew from the core and radiated to the surface, resulting in the formation of numerous voids. The crystallographic structure and phase purity of the precursor were confirmed by the XRD pattern (Fig. 1c). All the diffraction peaks of the precursor are in good agreement with those reported for $Fe(H_2O)_2[Ni(CN)_4]$ [38], showing that precursor possesses the same crystal structure as $Fe(H_2O)_2[Ni(CN)_4]$. The $Fe(H_2O)_2[Ni(CN)_4]$ precursor can be transformed into porous $Fe_2O_3/NiO$ microflower by annealing in air. The TG analysis showed that $Fe(H_2O)_2[Ni(CN)_4]$ precursor underwent two main decomposition steps (Fig. 1d). The first weight loss of 12% from room temperature to 100 °C indicates the loss of water molecules in the porous framework structure. The second weight loss of ca. 8% from 400 °C to 650 °C can be attributed to the oxidation of $CN^-$ into $CO_2$ and $N_2$. Based on the result, 650 °C was chosen as the calcination temperature in the experimental section.

Fig. 2a shows the XRD pattern of the calcination product of flower-like $Fe_2O_3/NiO$. All the diffraction peaks can be assigned to cubic phase $Fe_2O_3$ (JCPDS No: 02—1047) and cubic phase NiO (JCPDS No: 01—1239). No impurity peaks can be observed in the pattern, indicating the precursor has been completely transformed into $Fe_2O_3$ and NiO. Fig. 2b shows the EDS spectrum of the flower-like $Fe_2O_3/NiO$ composite, and the detected Fe/Ni atomic ratio in the
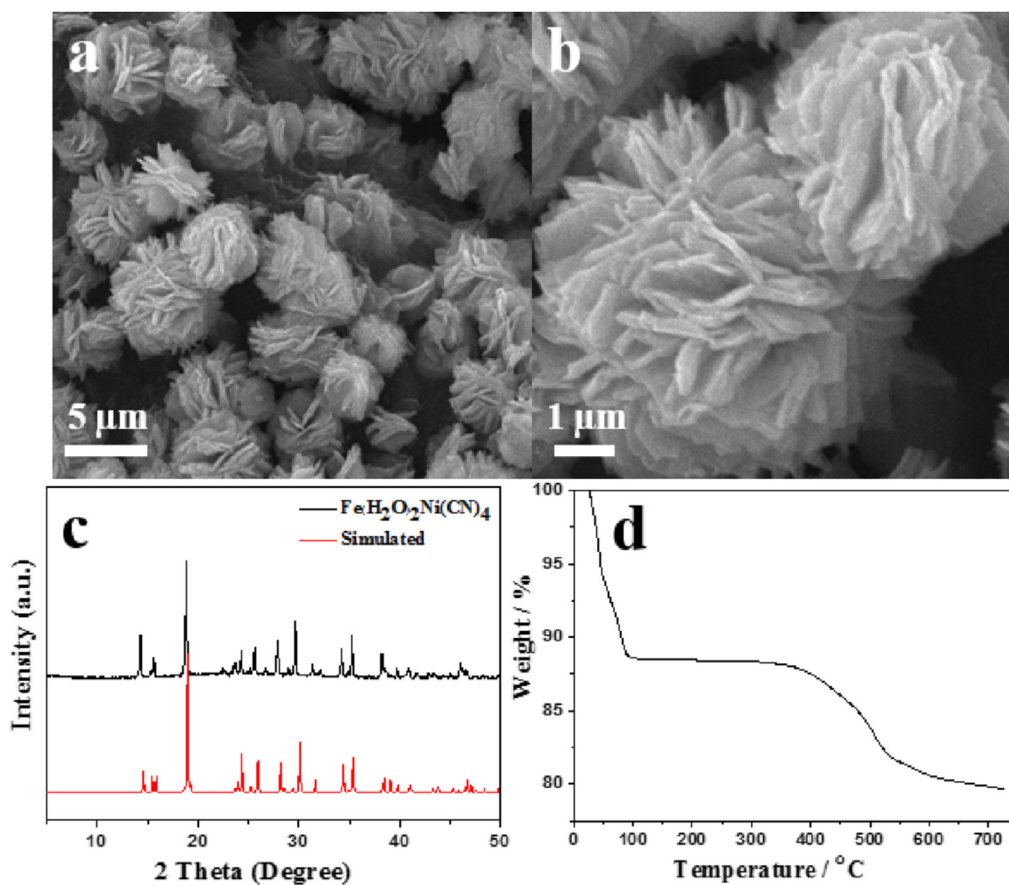
**Fig. 1.** (a) Low and (b) high magnification SEM images of the synthesized precursor. (c) XRD pattern and (d) TG curve of the Fe(H$_2$O)$_2$[Ni(CN)$_4$] precursor.



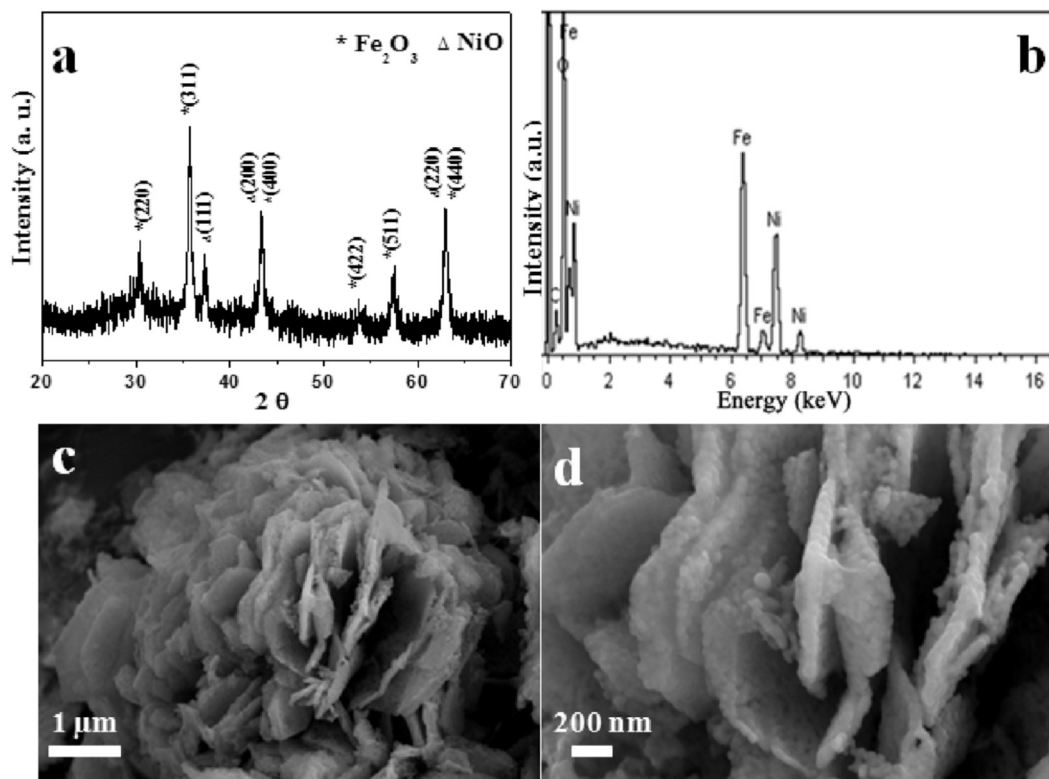**Fig. 2.** (a) XRD pattern, (b) EDX spectrum and (c, d) SEM images of the flower-like Fe$_2$O$_3$/NiO composite.

sample is almost 1:1, well consistent with that in the $Fe(H_2O)_2[Ni(CN)_4]$ precursor. Thus, the weight ratio of $Fe_2O_3$ to NiO in the composite is calculated to be 52:48 (Table S1). Fig. 2c and d shows the SEM images of the as-synthesized $Fe_2O_3$/NiO composite in different magnification. The sample exhibits flower-like morphology being highly consistent with the precursor, demonstrating that the morphology was well maintained during the calcination process. However, there is a little volume shrinkage due to the removal of water molecules and bridged $CN^-$ ions during the thermal treatment. The decomposition of $CN^-$ into $CO_2$ and $N_2$ can cause the formation of porous structure. The hierarchical microflowers are composed of many porous platelet-like petals with a thickness of about 80 nm.

The morphology and microstructure of the $Fe_2O_3$/NiO composite were further characterized using TEM and selected-area electron diffraction (SAED), which are shown in Fig. 3. The flower-like structures can be observed in Fig. 3a and b, which are assembled by porous platelets. Further, the platelets are composed of nanoparticles with a size of about 30 nm (Fig. 3c and d). The high resolution TEM image taken on the nanoparticles shows clear lattice fringes (Fig. 3e). The lattice spacing of 0.291 nm can be indexed to

the (220) plane of $Fe_2O_3$, while the lattice spacing of 0.207 nm can be assigned to the (200) plane of NiO. The SAED pattern (Fig. 3f) reveals the polycrystalline characteristics of the product, and the diffraction rings observed in the SAED pattern can be indexed as the (220) and (311) lattice planes of $Fe_2O_3$ as well as (200) and (220) lattice planes of NiO, well consistent with the XRD result. The EDS mapping images (Fig. 4) reveal that the elements of O, Fe and Ni are uniformly distributed in the whole structure, indicating the uniform distribution of the components of $Fe_2O_3$ and NiO in the porous hierarchical structure.

Inspired by the hierarchical porous microstructure of the $Fe_2O_3$/NiO composites, the specific surface area and pore size of the $Fe_2O_3$/NiO product were further analyzed by $N_2$ adsorption-desorption technique (Fig. 5). The typical pore size distribution is within 2−2.5 and 12−12.5 nm with a BET surface area of 32.31 $m^2$ $g^{-1}$. The single-point total volume of pore at $P/P_o = 0.988$ is 0.121 $cm^3$/g. These data further confirm a loose mesoporous structure of the prepared composite. It could be expected that as anode materials for LIBs, such a porous structure can provide a shortened pathway to increase the interfacial kinetics for ion/electron transport and accommodate the stress relaxation, resulting in the improvement
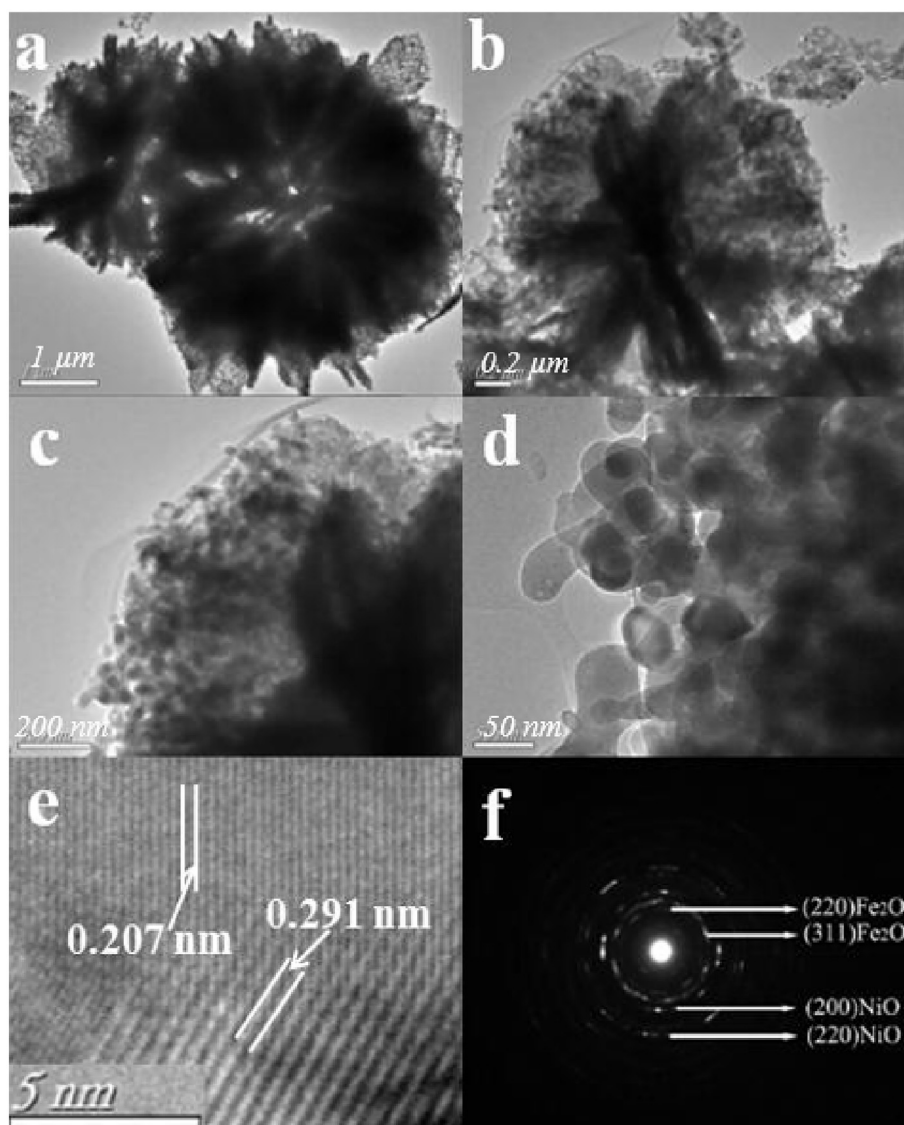


**Fig. 3.** (a–d) TEM images, (e) HRTEM image and (f) SAED pattern of the as-synthesized $Fe_2O_3$/NiO microflowers.
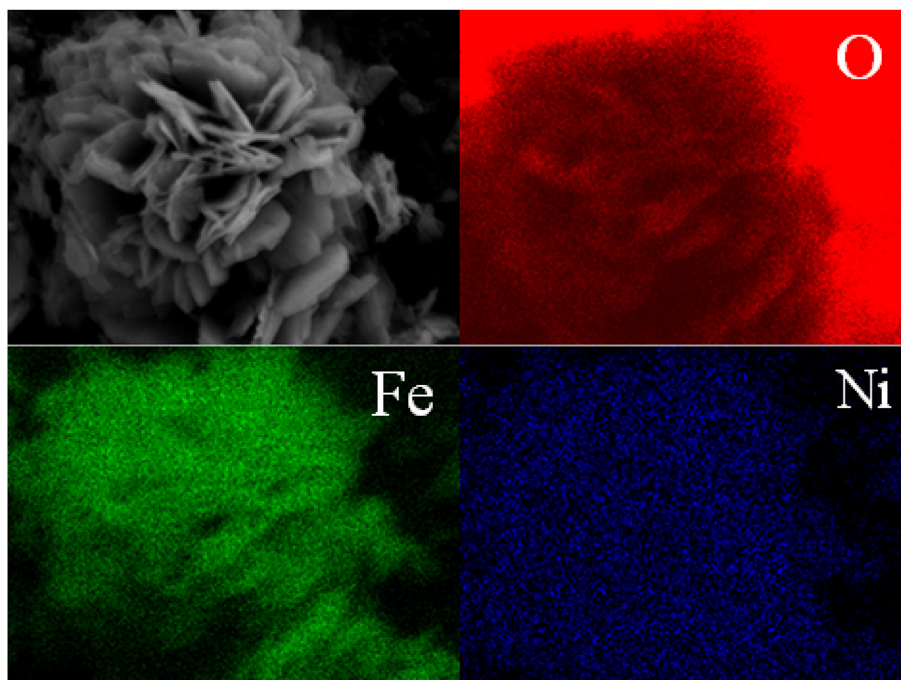
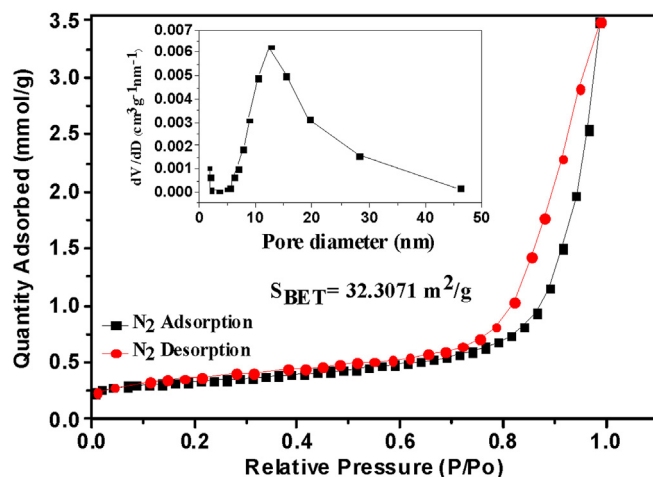**Fig. 4.** EDS mapping images for the elements of O, Fe and Ni.



**Fig. 5.** N$_2$ adsorption-desorption curves of the porous Fe$_2$O$_3$/NiO microflowers.

of reversible capacity and cycle performance.

### 3.2. Electrochemical performances of Fe$_2$O$_3$/NiO microflowers

Considering their unique structure and composition, the synthesized Fe$_2$O$_3$/NiO microflowers were investigated as anode materials for lithium-ion batteries. Fig. 6a shows the CV curves of Fe$_2$O$_3$/NiO microflowers in the first three cycles at a scan rate of 0.2 mV s$^{-1}$. During the first cathodic scan, an intense peak at 0.38 V and a sharp peak at 0.48 V could be respectively ascribed to the reduction of Fe$_2$O$_3$ to Fe and NiO to Ni nanograins, as well as the formation of Li$_2$O matrix and a solid electrolyte interface (SEI) film [39–41]. The two broad peaks at about 1.6 V and 2.2 V in the first anodic scan mainly correspond to the reversible oxidation of Fe to Fe$^{3+}$ and Ni to Ni$^{2+}$, respectively [42,43]. In the second cathodic cycle, the peaks shifted to higher voltage of 0.71 V and 0.83 V with

reduced peak currents. The peak shift to more positive potential is a common phenomenon for metal oxide anodes and is ascribed to the structure changes during the lithium insertion in the first cycle [44]. It should be noted that the curves overlap well in the following cycles, indicating that the hierarchical porous Fe$_2$O$_3$/NiO microflowers exhibit good electrochemical reversibility and cycle performance. The electrochemical reactions are as follows:
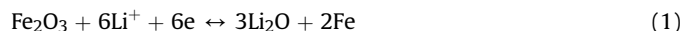
$$Fe_2O_3 + 6Li^+ + 6e \leftrightarrow 3Li_2O + 2Fe \tag{1}$$

$$NiO + 2Li^+ + 2e \leftrightarrow Li_2O + Ni \tag{2}$$

Fig. 6b shows the galvanostatic discharge-charge curves of Fe$_2$O$_3$/NiO microflower electrode at 100 mA g$^{-1}$ in the voltage window of 0.01–3 V for the first three and tenth cycles. There is a wide, steady discharging plateau at ca. 0.75 V in the first cycle, followed by a gradual voltage decrease. The specific capacity of the flower-like Fe$_2$O$_3$/NiO composite should depend on the mass ratio of Fe$_2$O$_3$ and NiO in the composite. The theoretical capacity (C) of the Fe$_2$O$_3$/NiO composite can be calculated on the contents of Fe$_2$O$_3$ and NiO as follows:

$$Ctheoretical = C_{Fe2O3} \times Fe_2O_3\ wt\% + C_{NiO} \times NiO\ wt\%$$
$$= 1007 \times 52\% + 718 \times 48\% = 867.2\ mAh\ g^{-1}$$

The initial discharge and charge capacities are 1652.6 mAh g$^{-1}$ and 1324.5 mAh g$^{-1}$, respectively, with high initial coulombic efficiency of 80.2%, showing the good reversibility of the electrode, which are much higher than the theoretical discharge capacity values of both Fe$_2$O$_3$ (1007 mAh g$^{-1}$) and NiO (718 mAh g$^{-1}$). It should be noted that the initial coulombic efficiency is much superior to the reported flower-like Fe$_2$O$_3$ anode with 75% and 64.8%, respectively [45,46]. The data are also higher than those of previously reported single metal oxides with other microstructures such as nanorods and nanotubes (Table S2) [9,22,47–49], indicating that the Fe$_2$O$_3$/NiO microflowers are superior to single metal oxides, which can be ascribed to the strong synergetic effect between
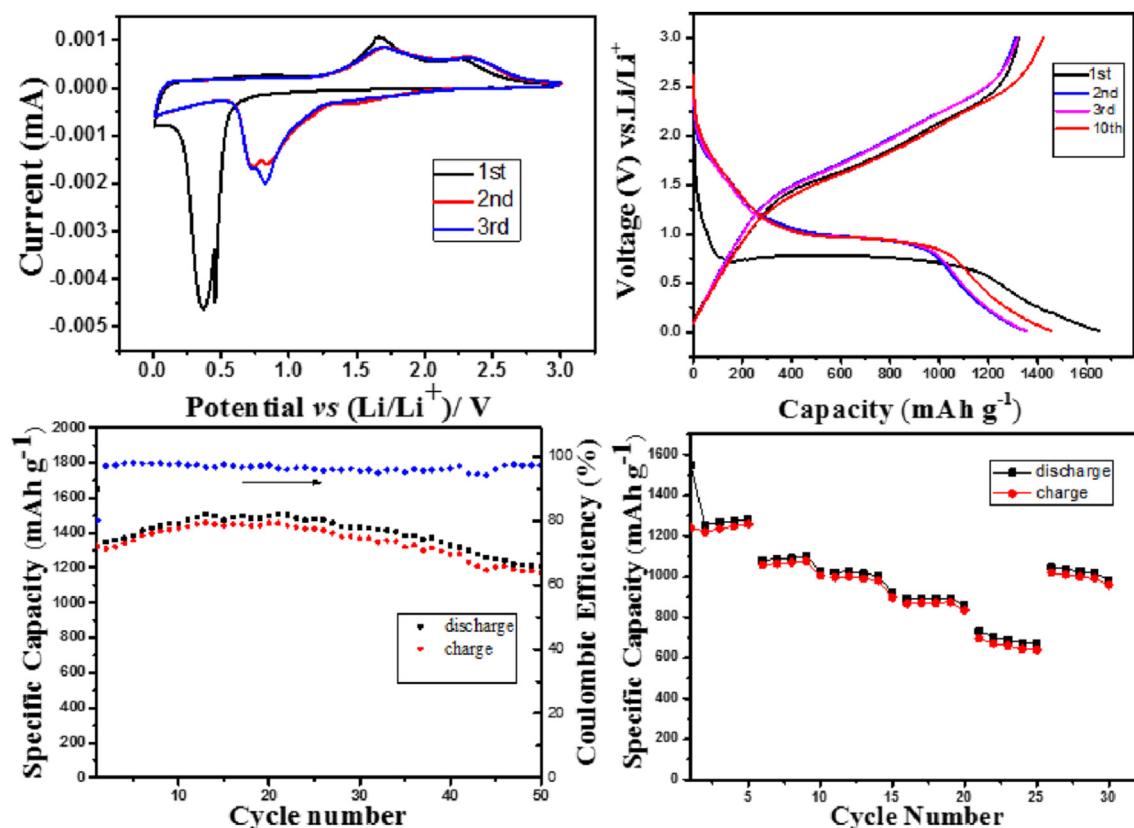
**Fig. 6.** (a) CV profiles at a sweep rate of 0.2 mV s$^{-1}$, (b) the first three and tenth discharge/charge voltage profiles in the range of 0.01−3.0 $vs$ (Li/Li$^+$) V at a rate of 100 mA g$^{-1}$, (c) cycle performances and coulombic efficiency at a rate of 100 mA g$^{-1}$, and (d) rate capabilities at different rate.

$Fe_2O_3$ and NiO in the composite. Reversible charge capacities of 1310.3 and 1320.7 mAh g$^{-1}$ were retained at the second and third cycle, respectively, suggesting the good cyclic stability. This improvement is ascribed to the porous nanostructures of $Fe_2O_3$/NiO, which could increase contact area between electrolyte and active materials, and improve electron and ion transport.

Cycling performances of hierarchical porous $Fe_2O_3$/NiO microflower at current density of 100 mA g$^{-1}$ are shown in Fig. 6c. It is worth noting that an increased charge capacity of 1456.8 mAh g$^{-1}$ can be achieved at the 20th cycle, corresponding to a coulombic efficiency of 97.01%, and then there is a gradual decline in the followed 30 cycles. At 50th cycle, the $Fe_2O_3$/NiO composite delivered a charge capacity of 1176.2 mAh g$^{-1}$ with capacity retention of 88.7% compared to the initial charge capacity. The cycle performance of the $Fe_2O_3$/NiO microflower is also reflected by EIS. The Nyquist plots of the $Fe_2O_3$/NiO microflower electrode before testing, after 20th cycle and 50th cycle are shown in Fig. S1. They are composed of a depressed semicircle in the high-frequency region and a sloping line in the low-frequency region. The intercept at the real axis at high frequency corresponds to the ohmic resistance, which represents the total resistance of the electrolyte, separator, and electrical contacts. The semicircle in the middle frequency range indicates the charge transfer resistance, and the inclined line in the low-frequency range represents the Warburg impedance. The larger semi-arc diameter suggests the larger charge transfer resistance. It can be clearly seen that the charge transfer resistances of the composite electrode decreased from 79.6 Ω of the initial cycle to 51.5 Ω at 20th cycle, then increased to 101.6 Ω for the 50th cycle, respectively. This result is also consistent with the cycle performances of $Fe_2O_3$/NiO composites. To further explore the cycle performances of $Fe_2O_3$/NiO electrodes, we also examined the

morphology and structural changes of the $Fe_2O_3$/NiO microflower after repeated Li$^+$ insertion/extraction. The coin cell electrochemically evaluated at 100 mA g$^{-1}$ for 50 cycles was disassembled and characterized by SEM (Fig. S2). Compared with Fig. 2c and d before cycling, it was found that the original microflower morphology and structure were retained after cycling. The improved cyclic stability and capacity retention of hierarchical porous $Fe_2O_3$/NiO microflowers may be ascribed to the special porous structure to accommodate the volume variation of $Fe_2O_3$/NiO, and the synergetic effect of $Fe_2O_3$ and NiO. High-rate electrochemical performances are also an important parameter for LIBs. Fig. 6d exhibits the excellent capacity retention of the $Fe_2O_3$/NiO microflowers at all rates. Even if the current density increases to 2 A g$^{-1}$, an average charge capacity of 693.6 mAh g$^{-1}$ is also maintained. More importantly, a high charge capacity of 1022.2 mAh g$^{-1}$ could be recovered when the current density was back to 100 mA g$^{-1}$, demonstrating good rate performance. In all, $Fe_2O_3$/NiO as anode material exhibits superior electrochemical performance, which could be attributed to the hierarchical porous structure of $Fe_2O_3$/NiO microflowers. Firstly, the stable porous hierarchical nanostructure could increase contact area and more active sites for electrochemical reactions, and enrich the lithium storage properties of materials. Meanwhile, the mechanical stress induced by the volume change during the lithium ion insertion/extraction may also be alleviated by sufficient void space. Finally, "synergistic effect" between $Fe_2O_3$ and NiO also helps to improve electrochemical capacity.

## 4. Conclusions

In summary, this work reports a hierarchical porous $Fe_2O_3$/NiO

microflower via thermal decomposition of a cyanide-metallic-framework. As an anode for LIBs, $Fe_2O_3$/NiO microflowers exhibit a remarkably improved electrochemical performance in terms of lithium storage capacity (1652.6 mAh g$^{-1}$ at 100 mA g$^{-1}$), cycling stability (1210.4 mAh g$^{-1}$ capacity retention at 50 cycles) and a good rate capability. The hierarchical porous microstructure of $Fe_2O_3$/NiO microflowers and the synergetic effect of $Fe_2O_3$ and NiO may contribute to the improved electrochemical performance. This work further demonstrates that the CMF-templates synthesis of metal oxides is an effective method for fabricating porous composite anode for advanced lithium ion batteries.

## Acknowledgment

## Appendix A. Supplementary data

Supplementary data related to this article can be found at http://dx.doi.org/10.1016/j.jallcom.2016.12.230.

## References

[1] J.J. Zhang, A.S. Yu, Sci. Bull. 60 (2015) 823—838.
[2] D. Larcher, J.M. Tarascon, Nat. Chem. 7 (2015) 19—29.
[3] S.N. Sun, Y. Nie, M.C. Sun, T. Liang, M.F. Sun, H.X. Yang, Mater. Lett. 176 (2016) 87—90.
[4] H.X. Yang, L. Li, J. Alloys Compd. 584 (2014) 76—80.
[5] H.B. Wu, J.S. Chen, X.W. Lou, H.H. Hong, J. Phys. Chem. C 115 (2011) 24605—24610.
[6] H.X. Yang, T.S. Song, S.K. Lee, H.K. Han, F. Xia, A. Devadoss, W. Sigmund, U.Y. Paik, Electrochim. Acta 91 (2014) 275—281.
[7] L. Xiao, D.Q. Wu, S. Han, Y.S. Huang, S. Li, M.Z. He, F. Zhang, X.L. Feng, ACS Appl. Mater. Inter 5 (2013) 3764—3769.
[8] M.C. Sun, M.F. Sun, H.X. Yang, W.H. Song, Y. Nie, S.N. Sun, Ceram. Int. (2017) 363—367.
[9] M.H. Chen, J.L. Liu, D.L. Chao, J. Wang, J.H. Yin, J.Y. Lin, H.J. Fan, Z.X. Shen, Nano Energy 9 (2014) 364—372.
[10] J.S. Cho, Y.J. Hong, J.H. Lee, Y.C. Kang, Nanoscale 7 (2015) 361, 8367.
[11] H.G. Wang, Y.Q. Zhou, Y. Shen, Y.H. Li, Q.H. Zuo, Q. Duan, Electrochim. Acta 158 (2015) 105—112.
[12] X.J. Ma, N.N. Wang, Y.T. Qian, Z.C. Bai, Mater. Lett. 168 (2016) 5—8.
[13] Z.Y. Fan, J. Liang, W. Yu, S.J. Ding, S.D. Cheng, G. Yang, Y.L. Wang, Y.X. Xi, K. Xi, R.V. Kumar, Nano Energy 16 (2015) 152—162.
[14] Y.F. Ma, L.M. Sheng, H.B. Zhao, K. An, L.M. Yu, J.Q. Xu, X.L. Zhao, Solid State Sci. 46 (2015) 49—55.
[15] H.L. Wang, L.F. Cui, Y. Yang, H.S. Casalongue, J.T. Robinson, Y.Y. Liang, Y. Cui, H.J. Dai, J. Am. Chem. Soc. 132 (2010) 13978—13980.
[16] N. Du, H. Zhang, B.D. Chen, X.Y. Ma, Z.H. Liu, J.B. Wu, D.R. Yang, Adv. Mater 19 (2007) 4505—4509.
[17] B. Yan, L. Chen, Y.J. Liu, G.X. Zhu, C.G. Wang, H. Zhang, G. Yang, H.T. Ye, A.H. Yuan, Crystengcomm 16 (2014) 10227—10234.
[18] X.Y. Yao, X. Xin, Y.M. Zhang, J. Wang, Z.P. Liu, X.X. Xu, J. Alloys Compd. 521 (2012) 95—100.
[19] L.M. Zhang, B. Yan, J.H. Zhang, Y.J. Liu, A.H. Yuan, Ceram. Int. 42 (2016) 5160—5170.
[20] H.X. Yang, Y. Wang, Y. Nie, S.N. Sun, T.Y. Yang, J. Compos. Mater. (2016), http://dx.doi.org/10.1177/0021998316644856.
[21] J.J. Zhang, T. Huang, Z.L. Liu, A.S. Yu, Electrochem. Commun. 29 (2013) 17—20.
[22] N.N. Wang, L. Chen, X.J. Ma, J. Yue, F. Niu, H.Y. Xu, J. Mater. Chem. A 2 (2014) 16847—16850.
[23] L. Zhang, H.B. Wu, S. Madhavi, H.H. Hng, X.W. Lou, J. Am, Chem. Soc. 134 (2012) 17388—17391.
[24] H. Wu, M. Xu, Y.C. Wang, G.F. Zheng, Nano Res. 6 (2013) 167—173.
[25] Y.S. Luo, J.S. Luo, W.W. Zhou, X.Y. Qi, H. Zhang, D.Y. Yu, C.M. Li, H.J. Fan, T. Yu, J. Mater. Chem. A 1 (2013) 273—281.
[26] N.A. Kyeremateng, C. Lebouin, P. Knauth, T. Djenizian, Electrochim. Acta 88 (2013) 814—820.
[27] X.H. Xia, J.P. Tu, Y.Q. Zhang, X.L. Wang, C.D. Gu, X.B. Zhao, H.J. Fan, ACS Nano 6 (2012) 5531—5538.
[28] P. Xiong, J. Zhu, X. Wang, J. Power Sources 294 (2015) 31—50.
[29] W.X. Guo, W.W. Sun, Y. Wang, ACS Nano 11 (2015) 11462—11471.
[30] Y. Yan, F.H. Du, X.P. Shen, Z.Y. Ji, H. Zhou, G.X. Zhu, Dalton Trans. 43 (2014) 17544—17550.
[31] J.K. Sun, Q. Xu, Energy Environ. Sci. 7 (2014) 2071—2100.
[32] L.N. Jin, Q. Liu, W.Y. Sun, CrystEngComm 16 (2014) 3816—3828.
[33] W. Xia, A. Mahmood, R.Q. Zou, Q. Xu, Energy Environ. Sci. 8 (2015) 1837—1866.
[34] Y.D. Chiang, M. Hu, Y. Kamachi, S. Ishihara, K. Takai, Y. Tsujimoto, K. Ariga, K.C.-W. Wu, Y. Yamauchi, Eur. J. Inorg. Chem. (2013) 3141—3145.
[35] M.B. Zakaria, M. Hu, M. Lmura, R.R. Salunkhe, N. Umezawa, H. Hamoudi, A.A. Belik, Y. Yamauchi, Chem. Eur. J. 20 (2014) 1—11.
[36] M.B. Zakaria, M. Hu, Y. Tsujimoto, Y. Sakka, N. Suzuki, M. Imura, S. Ishihara, K. Ariga, Y. Yamauchi, Chem. Asian J. 9 (2014) 1511—1514.
[37] G. Huang, L.L. Zhang, F.F. Zhang, L.M. Wang, Nanoscale 6 (2014) 5509—5515.
[38] R.Q. Lu, Y.Y. Chen, H. Zhou, A.H. Yuan, Acta Chim. Sinaca 68 (2010) 1199—1204.
[39] J.X. Zhu, Z.Y. Lu, M.O. Oo, H.H. Hng, J. Ma, H. Zhang, Q.Y. Yan, J. Mater. Chem. 21 (2011) 12770—12776.
[40] Q.Q. Xiong, Y. Lu, X.L. Wang, C.D. Gu, Y.Q. Qiao, J.P. Tu, J. Alloys Compd. 536 (2012) 219—225.
[41] X.H. Wang, Z.B. Yang, X.L. Sun, X.W. Li, D.S. Wang, P. Wang, D.Y. He, J. Mater. Chem. 21 (2011) 9988—9990.
[42] C.T. Cherian, J. Sundaramurthy, M.V. Reddy, P.S. Kumar, K. Mani, D. Pliszka, C.H. Sow, S. Ramakrishna, B.V.R. Chowdari, ACS Appl. Mater. Inter 5 (2013) 9957—9963.
[43] A.K. Mondal, S.Q. Chen, D.W. Su, K. Kretschmer, H. Liu, G.X. Wang, J. Alloys Compd. 648 (2015) 732—739.
[44] X.H. Wang, X.W. Li, X.L. Sun, F. Li, Q.M. Liu, Q. Wang, D.Y. He, J. Mater. Chem. 21 (2011) 3571—3573.
[45] V. Aravindan, P.S. Kumar, J. Sundaramurthy, W.C. Ling, S. Ramakrishna, S. Madhavi, J. Power Sources 227 (2013) 284—290.
[46] J.J. Zhang, Y.L. Chen, Y.F. Sun, T. Huang, A.S. Yu, RSC Adv. 3 (2013) 20639—20646.
[47] Y. Han, Y.J. Wang, L. Li, Y.P. Wang, L.F. Jiao, H.T. Yuan, S.X. Liu, Electrochim. Acta 56 (2011) 3175—3181.
[48] M.S. Balogun, Z.P. Wu, Y. Luo, W.T. Qiu, X.L. Fan, B. Long, M. Huang, P. Liu, Y.X. Tong, J. Power Sources 308 (2016) 7—17.
[49] Y.S. Wang, Y.F. Sun, X. Zhang, Q.Y. Zhu, Q. Zhang, W. Zhang, D. Hou, Y.H. Wen, J.X. Guo, Mater. Lett. 171 (2016) 125—128.